

Investigation of Flow Dynamics Around a Combination of Different Head Shapes of Spur Dikes

Sohail IQBAL, Ghufuran Ahmed PASHA*, Usman GHANI, Afzal AHMED, Rashid FAROOQ, Rizwan HAIDER

Abstract: Spur dikes are widely used as river training structures throughout the globe to improve navigation, strengthen flood protection, and save erodible banks. This study investigates the flow behaviour of multiple spurs using similar and different head shapes instead of adding an extra structure. The novelty of the study lies in finding out the best combination of head shapes among circular (C), rectangular (R), and triangular (T) that can reduce the responsible factors of scouring and erosion. The responsible factors for scour and erosion include high magnitude velocity, pressure, turbulence kinetic energy (*TKE*), Reynold stresses, and wall shear stresses. Nine combinations (3 same, i.e., CCC, RRR, and TTT and six different, i.e., CRC, CTC, RCR, RTR, TCT, TRT) of spurs were investigated using Computational Fluid Dynamics (CFD) code FLUENT. Firstly, in the analysis of similar head shapes, more reduction in the values of scour and erosion responsible factors were observed in CCC combination (20% in velocity, 45% in pressure, 41% in *TKE*, and 43% in normal Reynold stresses). Finally, the reduction was further improved in analysing different head shapes. The CTC combination showed the most effective results in reducing the prescribed factors (43% in velocity, 57% in pressure, 51% in *TKE*, and 54% in normal Reynold stresses) compared to both combinations of head shapes. Therefore, to protect riverbank and spur head failure due to severe turbulent flow, the combination of spurs (CTC) could be preferred.

Keywords: combination of spurs; numerical simulation; open channel flow; riverbank protection; wall shear stress

1 INTRODUCTION

For human protection, different hydraulic structures (river training works) are provided within a river to protect and manage river flow. The spur is among the most important and common river training hydraulic structures. There are various objectives, including energy dissipation [1, 2], for navigational [3, 4] backwards-facing step [5] and riverbank protection by diverting the flow from the riverbank towards the main flow [6]. However, their provision of either a single spur or a series depends on the situation. However, spurs are mostly provided in a series [7]. Therefore, before installing, it is very important to know the best combination of the spur in terms of size, shape, and orientation angle [8].

Studying the flow mechanism around different spurs is a very comprehensive and challenging topic in hydraulic engineering. From the past literature review, it can be observed that maximum study was related to the flow mechanism near the spur; however, a few found the best combination of the spur [9]. The permeable and impermeable spur with slope produced minimum turbulent kinetic energy (*TKE*) and shear stress. For riverbank protection, Mukherjee and Sarma [8] proposed the best combination of the spur. The numerical investigation was made separately by changing the size, position, and number of each spur combination. A numerical study was performed by Alauddin and Tsujimoto [7] to attain the main objectives, including enhancing scour in the main channel; to reduce the silt deposition within the spur dike field, and reducing maximum scour depth near the spur head.

Several experiments were performed and it was found that scour holes around the spur with side slopes can be reduced up to 60% compared with vertical-sided spurs. A 3D numerical model was developed by Tritthart et al. [10] to get the best combination of the spur for the River Danube in Austria. Four different combinations of spurs (A 1200 m long, two 500 m long, three 200 m. long, and two 300 m long repelling spurs, perpendicular to the river bank)

were made based on size, location, and number [3]. Based on overall performance (scouring, deposition, and stability), they found the best-fitted combination for the River Brahmaputra. Koutroul et al. [6] numerically investigated the optimal spacing between impermeable spurs to increase the bed shear stress within the main channel and reduce it near the spur dike field. It was found that spacing between the initial four emerged spurs should be less while it should be larger for the subsequent. Iqbal et al. [1] investigated the permeable spurs by varying permeability to enhance the carrying capacity of the river. A series of emerged and permeable spurs were investigated to minimize the scour-responsible factors, i.e., velocity and turbulence.

Flow 3-D software was used to investigate the flow dynamics around the series of spurs on a fixed bed [11]. It was found that the maximum magnitude of velocity and turbulence was found at the nose of the first spur. Moreover, vortices generated in the streamwise and spanwise directions were larger near the channel bed compared to the free water surface. The flow characteristics around permeable dike with different staggered pore angles [12] and making a combination of circular cylinders with impermeable dike [13] were investigated using FLUENT (ANSYS). Moreover, FLUENT (ANSYS) was previously also used to investigate flow structure for vegetation [14-15]. El-Rashedy et al. [16] experimentally investigated the scour mechanism around different head shapes (straight, Hockey, Mole, L shape, and T shape) of the spur. The combination of different shapes (I, T, L) of the spur was studied experimentally by Nayyer et al. [17]. They measured scour depth against different arrangements of spurs and found that T shape generated $0.3y$ (where y is flow depth) times less than other shapes when placed at a first location. Therefore, the best combination was L, T, T regarding minimum scouring. In another study, Nayyer et al. [18] studied scouring phenomena around the first spur due to the presence of the downstream spur. In this study, nine different arrangements were investigated by fixing the

position of the first spur. It was concluded that the best and optimal combination was the I, T, L series.

In Pakistan, different head shapes of spur have also been constructed at different locations for riverbank protection, including C shape, R shape and T shape, as shown in Fig. 1a to Fig. 1c. The head shapes may be rectangular [19-22], circular [23, 24], and tri-angular [9, 25-28]. The motivation for this study is to improve our understanding of flows around dikes combined with different head shapes. This study aims to get the most appropriate combination that minimizes the scour responsible factors (velocity, Pressure, TKE and Reynold stresses) without adding any extra hydraulic structure. Computational Fluid Dynamics (CFD) code FLUENT was used to simulate the flow by adopting a turbulence model known as Reynold's stress model (RSM).

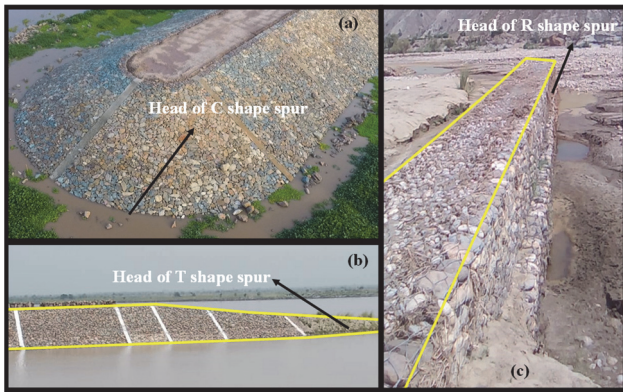


Figure 1 Different head shapes (C: Circular, R: Rectangular and T: Triangular) of spur which are present in (a) RMB of Head Baloki (b) At River Channab near Gujrat and (c) Baarhi Koh e SulamnTausa Sharif

The paper continues as follows: Section 2 is the research methodology that recalls the seven governing equations of the Reynold Stress model (RSM) used for present study, with the focus of experimental model validation and numerical simulation. Section 3 presents the results and discussion that includes distribution of depth averaged streamwise velocity, pressure, turbulent kinetic energy (TKE), Reynold normal stresses and wall shear stresses. Section 4 shows a detailed discussion of whole results achieved during this study. Section 5 finally concludes the paper.

2 METHODOLOGY

2.1 Governing Equations

For numerical modelling of steady and incompressible flow in an open channel, the continuity and Reynolds averaged Navier-Stokes equations were utilized. These equations can be written like this:

$$\frac{\partial U_i}{\partial X_i} = 0 \tag{1}$$

$$U_i \frac{\partial}{\partial X_j} (U_i) = \frac{v \partial}{\rho \partial X_j} \left(\frac{\partial U_i}{\partial X_j} + \frac{\partial U_j}{\partial X_i} \right) - \frac{1 \partial P}{\rho \partial X_{ij}} + (\overline{u_i' u_j'}) \tag{2}$$

The velocity components in the X_i direction is denoted by U_i . The velocity component in the X_j direction is U_j , the

kinematic viscosity is ν , the water density and the pressure are ρ and P respectively, and $\overline{u_i' u_j'}$ are the Reynold stresses. Eq. (3) depicts the Reynolds stresses transport in its most general form [29]. It comprises several terms that describe the partial differential equation used to transfer independent Reynolds stresses.

$$\frac{\partial R_{ij}}{\partial t} + C_{ij} = P_{ij} + D_{ij} - \varepsilon_{ij} + \Pi_{ij} + \Omega_{ij} \tag{3}$$

where $\frac{\partial R_{ij}}{\partial t}$ shows the change of Reynolds stresses with time, C_{ij} and D_{ij} are the transport of convection and stresses due to diffusion, P_{ij} is the rate of production, while ε_{ij} represents dissipation rate of stresses, Π_{ij} and Ω_{ij} are the transport of stresses because of pressure-strain, and rotation respectively.

The term convective is as follows:

$$C_{ij} = \frac{\partial (\rho U_k R_{ij})}{\partial X_k} \tag{4}$$

The Production term is:

$$P_{ij} = - \left(R_{im} \frac{\partial U_j}{\partial X_m} + R_{jm} \frac{\partial U_i}{\partial X_m} \right) \tag{5}$$

The term diffusion is just as follows:

$$D_{ij} = \frac{\partial}{\partial X_m} \left(\frac{\nu_t \partial R_{ij}}{\sigma_k \partial X_m} \right) \tag{6}$$

where $\nu_t = C_\mu k^2 / \varepsilon$; where $C_\mu = 0.09$; where $\sigma_k = 1$. The dissipation rate is similarly modelled on:

$$\varepsilon_{ij} = \frac{2}{3} \varepsilon \delta_{ij} \tag{7}$$

The Kronecker delta, which is given by $\delta_{ij} = 1$ if $i = j$ and $\delta_{ij} = 0$ if $i \neq j$. The Kronecker delta provides the rates of dissipation of TKE. The pressure phrase is provided by:

$$\Pi_{ij} = -C_1 \frac{\varepsilon}{k} \left(R_{ij} - \frac{2}{3} k \delta_{ij} \right) - C_2 \left(P_{ij} - \frac{2}{3} p \delta_{ij} \right) \tag{8}$$

$C_1 = 1.8$ and $C_2 = 1.8$. In addition, the TKE i.e., "k" can be modelled accordingly:

$$k = \frac{1}{2} \left(\overline{u_i'^2} + \overline{u_j'^2} + \overline{u_k'^2} \right) \tag{9}$$

Finally, the period of rotation is specified:

$$\Omega_{ij} = -2\omega_k \left(R_{jm} e_{ikm} + R_{im} e_{jkm} \right) \tag{10}$$

where ω_k and e_{ijk} are the rotation and altering vectors; e_{ijk} may be +1 or -1 when i, j and k are different in cyclic and anti-cyclic order respectively; and $e_{ijk} = 0$ if two integers are identical.

2.2 Experimental Domain with Rectangular Spurs

Experimental data of Brevis et al. [19] was used for the validation purpose in which domain was comprised of a series of the impermeable rectangular spurs. All the experiments were performed in 17 m long (L_c) and 1.3 m wide (B) flume having a slope of 1/1000 at the Institute of Hydromechanics, Germany. The laminated plastic was used to make the channel bed fixed and smooth, as shown in Fig. 2a. The distance between two spurs (W) was kept 24 cm and 48 cm for two aspect ratios ($\lambda = w/L$) 1 and 2 respectively. All the measurements were taken in the 24 cm length \times 45 cm width working domain using Particle Image Velocimeter (PIV) between two spurs marked with red colour as shown in Fig. 2a. Measuring locations $L1, L2$, and $L3$ were considered within the spur dike field with an equal distance of 6 cm from upstream to downstream in a spanwise direction. All the hydraulic conditions, including spur dimensions for the experimental domain, are given in Tab. 1.

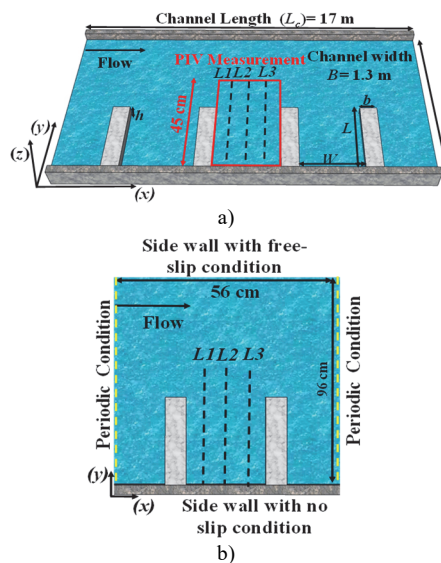


Figure 2 (a) Isometric view of the experimental setup [19] (b) Validation setup top view of the channel in which $L1, L2$, and $L3$ are the locations of measurements with aspect ratio $\lambda = W/L = 1$

Table 1 Experimental conditions of Brevis et al. [19]

Spur type	Rectangular and Impermeable	
Spur height, h	cm	7
Spur width, b	cm	4
Spur length, M	cm	24
Discharge, Q	l/s	9.75
Depth of water, z	cm	7
Average velocity, U	m/s	0.145
Froude number, Fr		0.13
Reynolds number for water depth, Re		7500

2.3 Numerical Model Setup with Boundary Conditions

For validation purposes, the numerical domain was reduced to 56 cm in length and 96 cm in width by providing periodic boundary conditions at the flow inlet and outlet.

All the other parameters, including channel width and spur dimensions, were kept unchanged.

Spurs were modelled as rigid rectangular bricks, as shown in Fig. 2b. ANSYS workbench was utilized for the meshing of the numerical model. The unstructured mesh (tri-pave) with tetrahedral elements was used, having $108 \times 524 \times 124$ nodes in the streamwise, transverse and vertical directions generating almost 7 million grid points. To confirm the accuracy of the CFD simulations, the mesh independence test was also performed. Three computational grids a coarse mesh with 3.1 million grids, a medium mesh with 7 million grids, and a fine mesh with 11.2 million grids were initially utilized to ensure mesh independence. The major velocities differed between the coarse and medium meshes by around 4.5 percent, whereas the findings between the medium and fine meshes varied by about 0.9 percent, which was not statistically significant. As a consequence, a mesh with 7 million grids and a 0.3 cm minimum interval size was selected... The periodic boundary condition was assigned to ensure uniform flow behaviour at both locations, i.e., inlet and outlet of the domain. The discharge and flow depth in the channel were 9.75 L/s and 0.07 m, respectively. The symmetry boundary condition for the free surface was assigned; however, the bed, sidewalls, and spurs were assigned using the no-slip condition and standard wall function as used by previous researchers [1, 30, 31].

For simulation and post-processing, CFD code FLUENT was used. A Reynolds stress model (RSM) was used for turbulence closure. A SIMPLE (Semi-Implicit Method for Pressure Linked Equations) algorithm was used to achieve Pressure-velocity coupling. The criteria for the solution were supposed to be convergent when residuals were set at 1×10^{-6} .

2.4 Model Validation

The experimental results of Brevis et al. [19] and numerical results of depth-averaged spanwise (v) velocity were compared at specified locations ($L1, L2$, and $L3$) and are shown in Fig. 3. The measuring locations are at 6 cm, 12 cm, and 18 cm from the upstream (u/s) to downstream (d/s) spur. At the x -axis, spanwise velocity was normalized with initial velocity $U = Q/BZ$, in which Q represents discharge and BZ represents the area. The Y -axis (total channel width) was made dimensionless by dividing it by spur length. The dashed line separates mainstream ($Y/L = 1 - 1.6$) from spur dike field ($Y/L = 0 - 1$). Mass and momentum exchange behaviour divide the whole channel into two zones, i.e. mainstream and spur dike field [32, 33]. All the velocities were captured at half of the channel depth ($z = 3.5$ cm). The two results (experimental and numerical) are in good agreement, as shown in Fig. 3. From the validation, the computational domain can recreate actual results in a rectangular open channel of this sort and, therefore, can be utilized for simulation.

In Fig. 3, both experimental and numerical spanwise velocity showed zero values in the mainstream, i.e., $Y/L = 1 - 1.6$ at all three locations ($L1, L2$, and $L3$). In the spur dike field ($Y/L = 0 - 1$), velocity values showed an inflation trend at $L1$ due to the high magnitude of mass and momentum exchange behaviour.

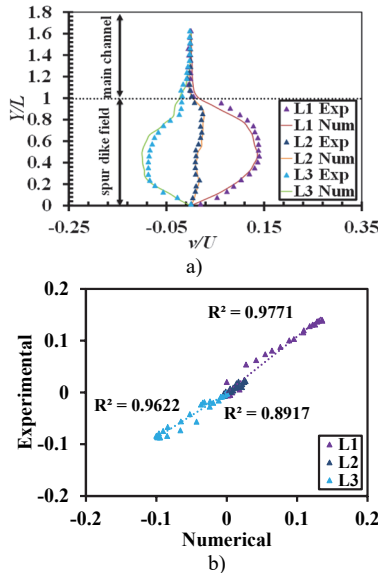


Figure 3 (a) Comparison of experimental [19] and numerical results for spanwise velocity v/U at three different locations ($L1$, $L2$, and $L3$). The dashed line represents the edge of the spurs. (b) Trend line with R^2 values to quantify the error

At $L2$, velocity showed zero magnitude due to the recirculation eye formed in the mid of the spur dike field. The negative values of spanwise velocity at $L3$ were due to recirculation, which moves from downstream to upstream. These results were verified by Iqbal et al.[1]. Hence the present validated computational domain can be utilized for numerical simulation.

2.5 Numerical Simulation

For the present numerical model, 84 cm long and 96 cm wide domain contains three impermeable spurs with the

same and different head shapes (Fig. 4). All the other hydraulic and geometric conditions (given in Tab. 2) were kept the same as used for the validation purpose (Sec 2.3). The combination of three impermeable spurs with the same (three cases) and different (six cases) head shapes was used for numerical simulation. The schematic diagram to represent measuring locations $M1$, $M2$ and $M3$ is shown in Fig. 4. The specified measuring location was selected at just u/s of each spur because high scour depth responsible factors (velocity, pressures, TKE , Reynolds stresses) generated maximum magnitude at this location [17]. A tri-pave unstructured mesh was selected with an interval size of 0.2 cm for this study. It generated $128 \times 608 \times 154$ nodes in streamwise, spanwise, and depth wise directions, respectively, with 12 million grid points. All the cases (C-1 to C-9 can be seen in Tab. 2) represent non-submerged spur cases.

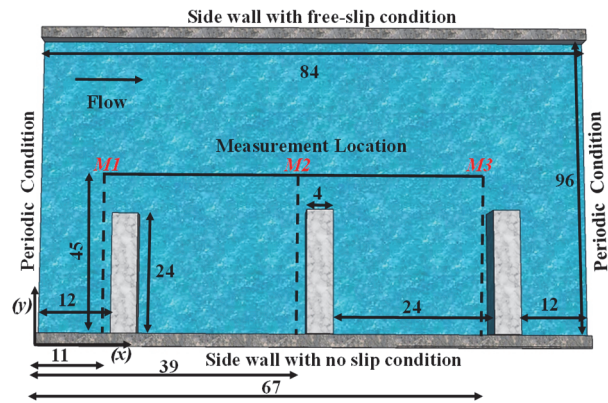


Figure 4 The schematic view of the computational domain used for numerical simulation with three measuring locations $M1$, $M2$ and $M3$. All units are in cm

Table 2 Flow conditions used for numerical simulations, where C-1 to C-9 represents case 1 to case 9

Cases	C-1	C-2	C-3	C-4	C-5	C-6	C-7	C-8	C-9
Types of Spurs	CCC	RRR	TTT	CRC	CTC	RCR	RTR	TCT	TRT
Measuring location	$M1, M2, M3$								
submergence	Non-submergence								
Discharge, $Q / L/s$	9.75								
Flow depth, z / cm	7								
Initial Velocity, $U / m/s$	0.145								
Froude number, Fr	0.13								
Reynolds number, Re	10000								

3 RESULTS

3.1 Depth-Averaged Streamwise Velocity Distribution

Fig. 5 represents the normalized depth-averaged streamwise velocity distribution (u/U) in the spanwise direction. The computing locations ($M1$, $M2$, and $M3$) can be important while observing the flow behaviour at just u/s of spurs. The spanwise dimension (Y) of the computational domain was normalized with the length of the spur, while mean-streamwise velocity (u) was normalized with initial velocity (U).

The velocity profile (u/U) starts from the right bank of the channel towards the left bank, almost equal to zero up to $Y/L = 0.8$ for all the specified locations. Because the flow velocity within the spur dike field is almost equal to zero, it has sufficient values near the head of the spur ($Y/L = 1$). It began to increase towards the main flow ($Y/L = 0.8-1.8$). The increasing trend of velocity (u/U) from the right bank

to the left bank remained the same. However, it showed fluctuations at the locations of the spur head, i.e., $Y/L = 1$.

Fig. 5a shows the higher value of mean streamwise velocity for R shape in both zones, i.e., within the spur dike field and the main channel. The highest values in C-2 were due to the corner (edge) of the rectangular shape that faces the high flow. Yarahmdi et al [9] found that the R shape spur has a maximum depth of scour hole at u/s , while for the T shape, it is vice versa. So, it means that the T shape is better compared with R in the case of the depth of scourhole. The C-shaped spur is also studied in the present study, and the results are compared with T and R shapes. The circular head shapes gave minimum velocity near the head ($Y/L = 1$) to generate a minimum scour hole. Due to the circular shape of the spur, flow smoothly moves downward without generating a high-velocity impact on the head. In comparison, high flow velocity increases the scouring around the spur [34]. The highest value of depth-

averaged velocity was for C-7 measured at $M1$, $M2$ and $M3$. At $Y/L = 1$, the maximum reduction of depth-averaged velocity was 20% for C-1, while for C-5, it was 43% at $M2$.

3.2 Pressure Distribution

The pressure distribution for C-1to C-3 and C-4 to C-9 is shown in Fig. 6a and Fig. 6b, respectively, at $M1$, $M2$, and $M3$. As flow approaches to spur, the velocity head is converted to a pressure head which causes bed scouring due to a horseshoe vortex [17]. Fig. 6a showed that C-2 has the highest pressure value near the nose of the spur compared to C-1 and C-3. The maximum pressure at the u/s of each spur in the RRR combination was generated due to the maximum flow obstruction that generates the main horseshoe vortex and bed shear stress [24]. The higher magnitude of pressure will result in higher thrust on the

head, which ultimately causes failure of the spur partly or fully [32]. From C-4 to C-9 (Fig. 6b), it was observed that circular shapes combined with triangular give better results compared to rectangular head shapes. In RCR and RTR, maximum pressure was at the u/s of the 1st and 2nd spur. When a C-shaped spur was combined with a T-shaped (CTC), a low flow field was generated due to C and T head shapes.

In other words, the higher the flow field, the greater the bed shear stress and pressure. These two factors will directly generate the scouring at the u/s of each spur. Koken and Gogus [24] observed high bed shear stress and horseshoe vertex in terms of the larger length of a spur. Thus, the circular shape generates a minimum magnitude of pressure on the u/s side, which remained the same even after the d/s .

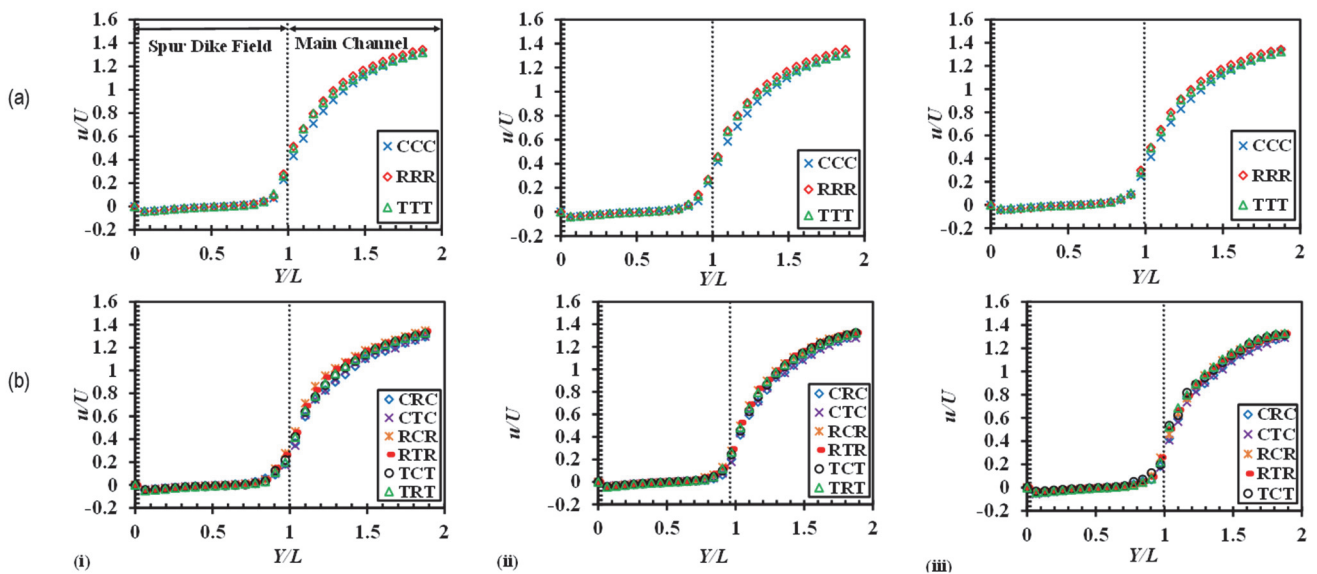


Figure 5 Distribution of mean streamwise velocity for the combination of similar (Fig. 5a) and different (Fig. 5b) head shapes of spur at measuring locations (i) $M1$, (ii) $M2$ and (iii) $M3$

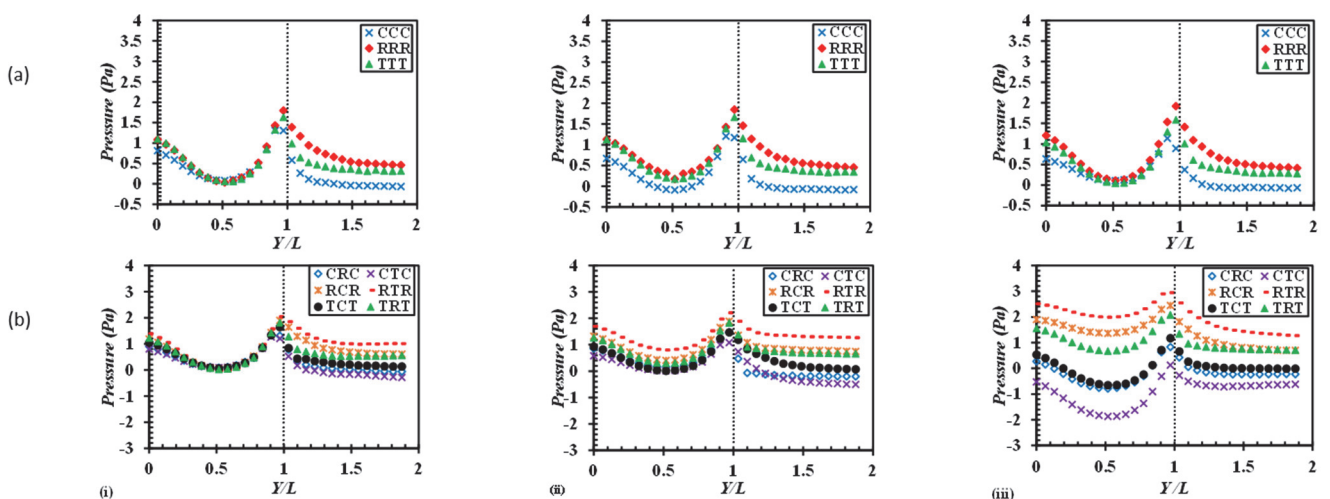


Figure 6 Deviations of depth-averaged pressure at critical locations $M1$ (Fig. 6i), $M2$ (Fig. 6ii) and $M3$ (Fig. 6iii) for similar (Fig. 6a) and different (Fig. 6b) head shapes of the spur

3.3 Turbulent Kinetic Energy

Fig. 7 represents the depth average TKE in the spanwise direction at $M1$, $M2$, and $M3$. To make it non-

dimensional, TKE was divided with U^2 . At the location of the spur head, TKE showed higher values for the C-2. However, TKE gave the same inflation trend for all combinations (C1-C9). At $M2$, the TKE reduced up to 41%

for C-1 compared to the highest value of C-2. Similarly, in the combination of different head shapes, the reduction was further increased when compared at $M1$ up to 51% for C-5. The circular head shapes generate less turbulence as compared to triangular and rectangular head shapes. The larger turbulence in the case of rectangular is due to the u/s corner that directly bears the flow. At the same time, it is reduced in the case of C-3 because the corner further shifted towards the d/s side [25].

After combining the C shape with R and T, it gives better, C-5 gives the best result at $M1$, $M2$ and $M3$ because two C shapes were combined with T and R shapes. Moreover, C-8 and C-9 also gave better results compared to C-6 and C-7 because in C-8 and C-9 two T shapes combined with the C and R head shapes of spurs, respectively.

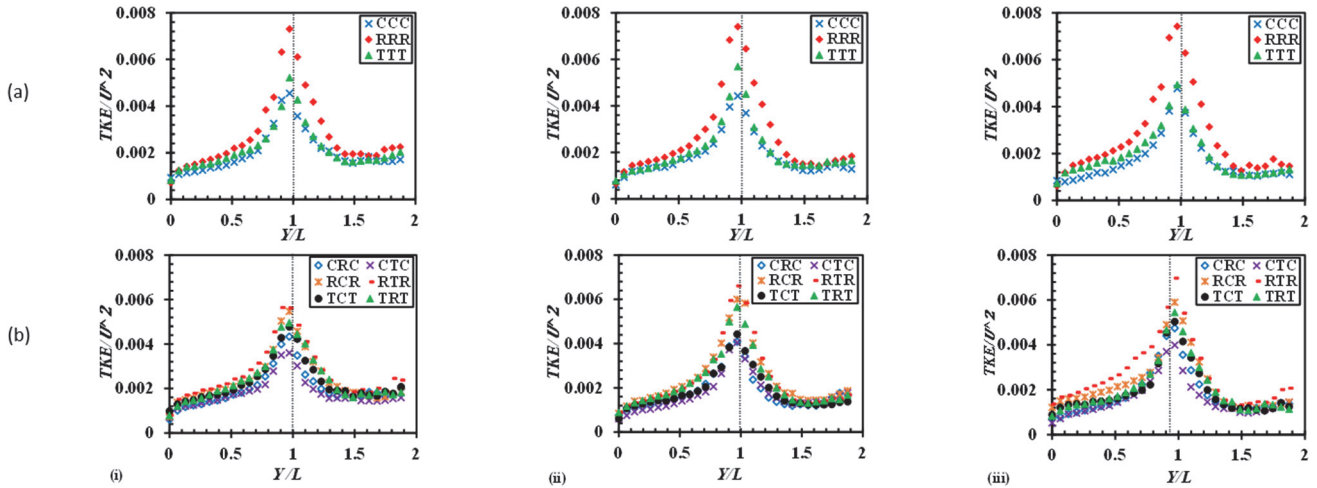


Figure 7 Distribution of depth-averaged TKE at $M1$ (Fig. 7i), $M2$ (Fig. 7ii) and $M3$ (Fig. 7iii) for similar (Fig. 7a) and different (Fig. 7b) head shapes of spur.

3.4 Turbulent Kinetic Energy Contours

The contours of TKE were taken in the presence of three emerged impermeable spurs, as shown in Fig. 8. In Fig. 8b series of R shape, spur showed higher turbulence at just u/s of the spur. However, in the case of C (Fig. 8a) and T shape (Fig. 8c), the higher turbulence was not limited to just u/s but shifted towards the d/s direction. So higher turbulence is responsible for higher scour depth in moveable bed cases side after the location of the head of the spur. So, in this study, the circular head shape gives minimum values in the combination of the same and different head shapes. The depth-averaged pressure was reduced up to 45% for C-1 and it was 57% for C-5 measured at $M3$ when compared to C-2 [17]. In different head shapes, C shape plays a vital role in turbulence

reduction without adding any extra structure like protective spur [17, 36], pile groups [37, 38], hollow cylinders in impermeable spur to make it permeable [1] and collar around the spur [36, 39].

When R and T spurs are combined with C shaped, it further reduces high turbulence, as shown in Fig. 8d & Fig. 8e. The reduction of TKE was more in C-4 and C-5 compared to C-1. Even in the combination C and T provided in between R shape, it resulted in a higher magnitude of TKE . The C-8 and C-9 gave better results compared to C-6 and C-7 due to the presence of two T shape spurs with R and C. As two R shapes could not reduce the magnitude of TKE that is why higher turbulence can be observed in both combinations (C-6 and C-7).

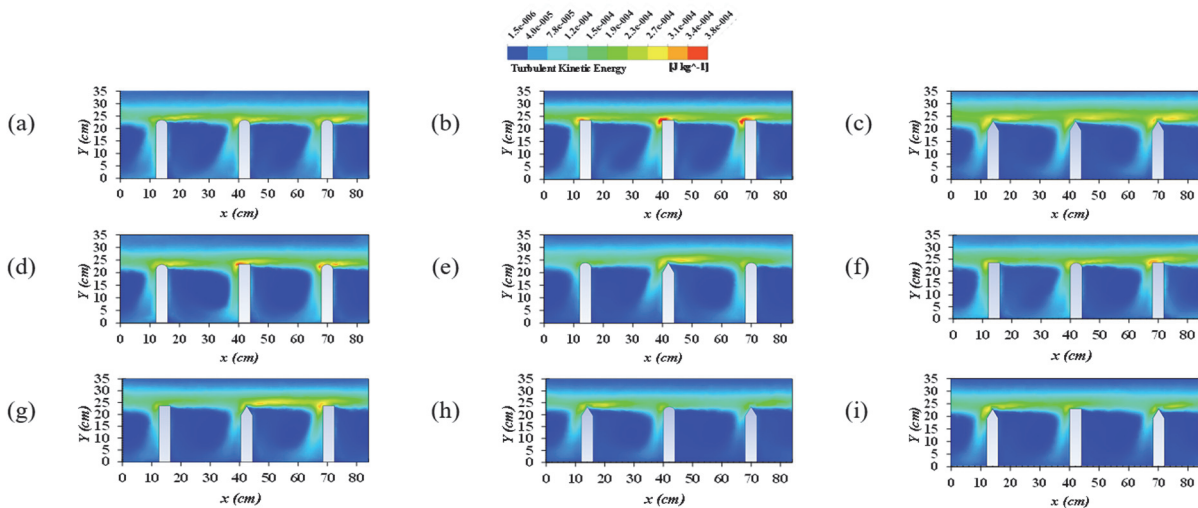


Figure 8 Contour plot of TKE distribution for cases C1-C3 (Fig. 8a to Fig. 8c) and for cases C4-C9 (Fig. 8d to Fig. 8i)

3.5 Reynold Normal Stress Distribution

The spanwise distribution of normal Reynolds stresses at specified measuring locations for all cases (C-1 to C-9) is shown in Fig. 9. The normal stresses were made dimensionless concerning U^2 , while the width of the channel (Y) was normalized with spur length. In Fig. 9, $u'u'$, represent the normal Reynolds stress fluctuations in a streamwise direction. The point of inflation, i.e., $Y/L = 1$, was the same for all cases (C-1 to C-9). Both C-2 and C-7 showed larger fluctuations, whereas these stresses were less for C1 and C-5 at $M1$, $M2$, and $M3$.

The normal Reynolds stresses ($u'u'$) remained uniform from the start of the right bank, i.e., ($Y/L = 0$) up to $Y/L = 0.5$ and from $Y/L = 1.5$ to 1.8. For all cases, the peak

values of Reynolds normal stresses occurred at the head of the spur ($Y/L = 1$) as maximum mass and momentum exchange behaviour occurred around the head shape of the spur. Then, the Reynold stresses values increased from $Y/L = 0.5$ to $Y/L = 1.5$. The resulted profile shapes for normal Reynold stresses were the same under the combinations of the same and different head shapes of the spur, but with variation in magnitude, specifically, peak values at the location of spur head i.e., $Y/L = 1$ were observed. In the case of C-1 to C3, reductions in $u'u'$, were up to 43%, for C-1 at $M3$, respectively. While in the case of C-4 to C-9, reduction in $u'u'$ was up to 54% for C-5 at $M2$.

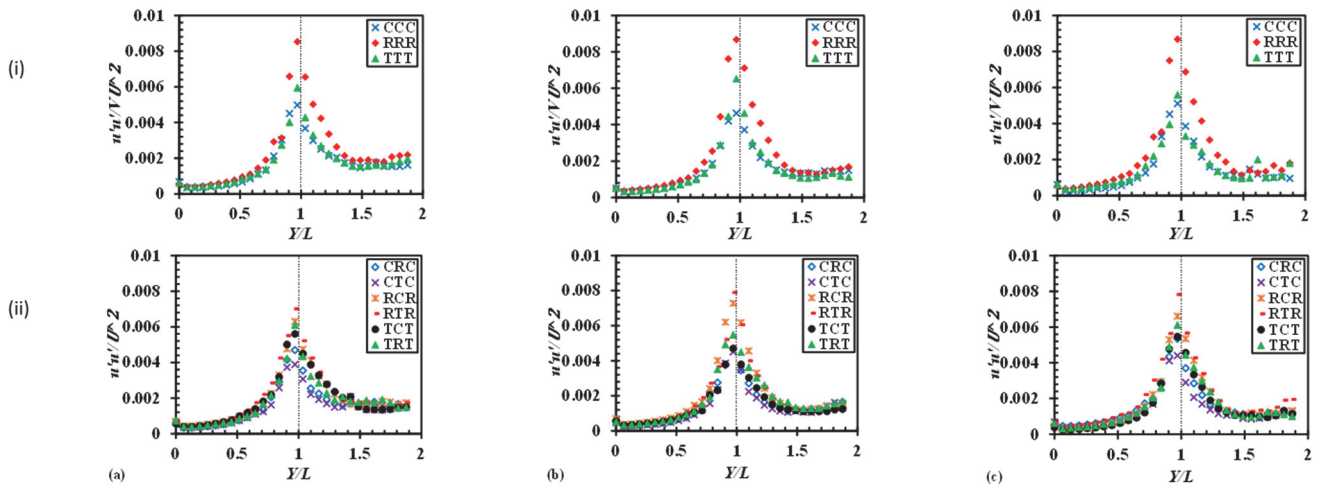


Figure 9 Distribution of simulated streamwise normal Reynolds stresses " $u'u'$ " at specified positions $M1$ (a) $M2$ (b) and $M3$ (c) for cases C1-C3 (i) and C4-C9 (ii)

3.6 Wall Shear Stress Distribution

Fig. 10 represents the wall shear stress percentage reduction for the combination of the same and different head shapes of the spur to achieve the minimum wall shear stresses. The optimum combination is the one without adding extra structure that achieves maximum bed and minimum wall shear stress [6]. The wall shear stress was measured at the right bank of the channel along the flow direction. In the spur dike field, i.e., $Y/L = 0 - 1$, C-1 gave lower values of wall shear than C-2 and C-3. The C-2 generates high flow velocity due to larger flow resistance at the head, which is ultimately responsible for higher values. The low flow in the spur dike field is maintained by placing different arrangements. The maximum reduction of wall shear stress was 40% in both spur dike fields for C-1.

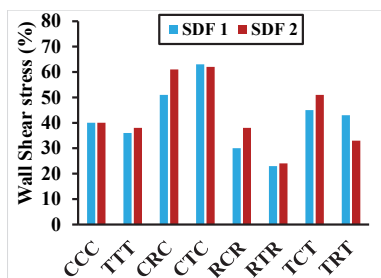


Figure 10 Wall shear stress percentage reduction for C-1 to C-9 measured along the right bank of the channel in spur dike field 1 and spur dike field 2

Because the C-shaped spur generates a slow flow field due to its head shape, according to Yarahmadi et al. [9], an R shaped-spur generates a high flow field compared to a T shape. In the case of the combination of different head shapes, the reduction was 63% and 62% for the C-5 in spur dike field 1 and spur dike field 2, respectively. So optimum combination of the same and different head shapes of the spur was C-1 and C-5, respectively.

4 DISCUSSION

The comparison result of different flow parameters measured at $z = 3.5$ cm is shown in Fig. 11. Different scour regions can be identified by investigating the position of the stresses and pressure [24]. The flow approaches to the spur have maximum pressure and TKE values, and the spur head was the focus of high-intensity flow. So maximum values of velocity, pressure, TKE , and Reynolds stresses were found at the tip of each spur. The reduction of these factors can be observed in Fig. 11, which was calculated by comparing the highest values of C-2.

However, the maximum reduction was observed due to a circular shape, triangular and rectangular spur. The maximum reduction in similar head shapes was CCC (17%, 18% and 20%), while in different shapes, CTC (38%, 43% and 39%) gave better results (Fig. 11a). In CRC, the mean velocity reduction at $M2$ was less compared to $M1$ because at $M2$ R-shaped spur generated high flow

velocity, while this flow measured at $M3$ the reduction increased due to gentle movement of flow around C shaped spur [25]. In RTR, the larger reduction at $M2$ was less compared to $M1$ and $M3$ because two R-shaped spurs generate a high flow field that diverts the whole flow towards the middle of the channel.

The pressure reduction (Fig. 11b) was minimum in the RCR and RTR in different combinations, while it was the same in TTT at $M1$, $M2$ and $M3$. It is due to two R-shaped spurs with a larger area of flow contact than T and C shaped spurs. Hence, flow exerted a high impact on the R shaped, which generated the strongest vortices around the R shaped spur, and ultimately higher magnitude of pressure can be observed. The pressure reduction for CRC and CTC was

31%, 53%, 22% and 36%, 57%, and 43% at $M1$, $M2$ and $M3$, respectively. The same flow behaviour was observed in turbulence (TKE and Reynold stresses) as shown in Fig. 11c to Fig. 11f. The TKE and Reynold normal stresses showed an inflation trend at $M2$ for CRC and CTC because, at $M2$, turbulence due to the C-shaped spur (at $M1$) generated minimum values. Due to the narrowing flow cross-section near the T [25] and C shaped spur, low turbulence values were observed. Similarly, lower values at $M2$ for RCR, RTR and TCT were observed due to the presence of C and T shaped spur dike upstream of these spurs, which are responsible for reducing TKE and Reynold stresses.

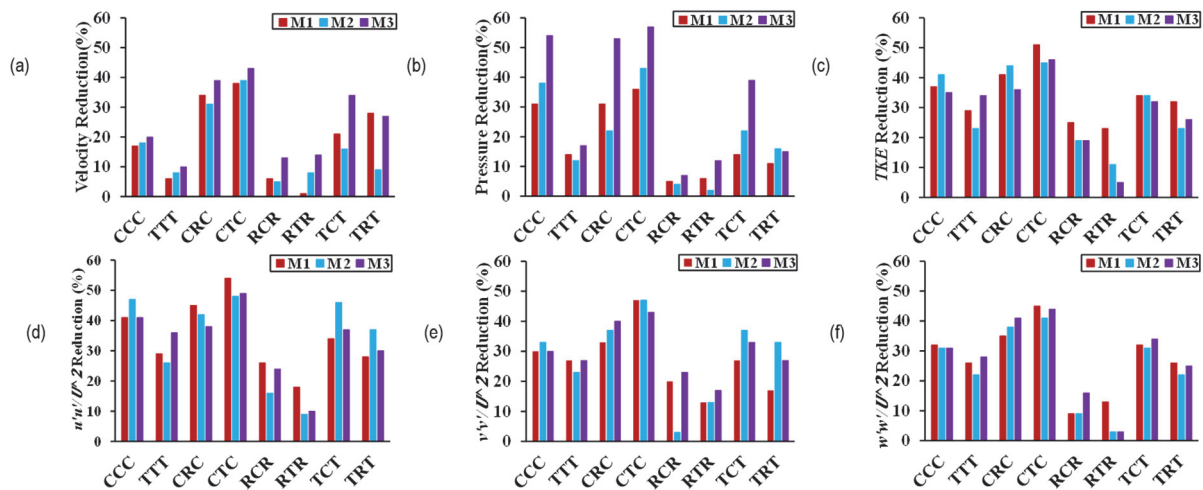


Figure 11 The comparison results of reduction of (a) depth-averaged dimensionless streamwise velocity, (b) pressure (c) TKE , dimensionless (d) streamwise, (e) spanwise, and (f) depthwise, normal Reynold stresses in % at $M1$, $M2$ and $M3$

5 CONCLUSIONS

This study investigated three-dimensional flow around the combination of similar (CCC, RRR and TTT) and different (CRC, CTC, RCR, RTR, TCT, TRT) head shapes of the spur CFD code ANSYS FLUENT. The core objective of the present work was to minimize the responsible factors of scour and erosion. The reduction of the results for all the responsible factors of scour and erosion was observed for both (similar and different) head shapes. The main concluding remarks of the current study are as follows:

- (1) The spur head is the key point where the mass and momentum exchange occurs. Depth averaged streamwise velocity showed the lowest magnitude in CTC combination measured at the head of all three emerged impermeable spurs. This is due to the presence of C shapes spur, which minimizes the high-velocity magnitude without making any changes in the spur.
- (2) C shaped spur has less area of greater magnitude of high shear stress and turbulence compared to T and R-shaped spurs. In the same head shape combination, the reduction of velocity, pressure, TKE and normal Reynolds stresses were up to 20%, 45%, 41%, and 43%, respectively. Placing C shaped spurs (CRC and CTC) in different shapes at first and third locations has a greater impact on flow structure. Due to this position of C shaped spur, 43% of streamwise velocity, 57% of pressure, 51% of TKE and

54% of normal Reynold stress, even placing it at the second position, gave better results.

- (3) The high magnitude of pressure at the u/s of the C-shaped spur located at the first and third position showed lower values compared to T-shaped and R-shaped combinations. This combination phenomenon may help reduce scour area, resulting in minimum erosion volume.
- (4) Wall shear stresses showed that due to horizontal vortex formation around R and T shape spurs, higher wall shear stress was generated. In similar head shapes (CCC), the reduction was 40% in each spur dike field, while 63% and 62% in the first and second spur dike field, respectively, in CTC combination of different head shapes.

These results are crucial for creating a practical scour mitigation plan for scour-prone locations. In the future a detailed study can be conducted to investigate the flow pattern inside the spur dike. Moreover, the reattachment length pattern formed at the downstream of dikes due to different head shapes of dikes can be conducted experimentally as well as numerically.

6 REFERENCES

- [1] Iqbal, S., Pasha, G. A., Ghani, U., Ullah, M. K., & Ahmed, A. (2021). Flow dynamics around permeable spur dike in a rectangular channel. *Arabian Journal for Science and Engineering*, 46(5), 4999-5011. <https://doi.org/10.1007/s13369-020-05205-y>
- [2] Karami, H., Basser, H., Ardeshtir, A., & Hosseini, S. H.

- (2012). Verification of numerical study of scour around spur dikes using experimental data. *Water and Environment Journal*, 28(1), 124-134. <https://doi.org/10.1111/wej.12019>
- [3] Karmaker, T. & Dutta, S. (2016). Prediction of short-term morphological change in large braided river using 2D numerical model. *Journal of Hydraulic Engineering*, 142(10). [https://doi.org/10.1061/\(asce\)hy.1943-7900.0001167](https://doi.org/10.1061/(asce)hy.1943-7900.0001167)
- [4] Azinfar, H. & Kells, J. A. (2009). Flow resistance due to a single spur dike in an open channel. *Journal of Hydraulic Research*, 47(6), 755-763. <https://doi.org/10.3826/jhr.2009.3327>
- [5] Pasha, G. A., Tanaka, N., Yagisawa, J., & Achmad, F. N. (2018). Tsunami mitigation by combination of coastal vegetation and a backward-facing step. *Coastal Engineering Journal*, 60(1), 104-125. <https://doi.org/10.1080/21664250.2018.1437014>
- [6] Koutrouveli, T. I., Dimas, A. A., Fourniotis, N. T., & Demetropoulos, A. C. (2018). Groyne spacing role on the effective control of wall shear stress in open-channel flow. *Journal of Hydraulic Research*, 57(2), 167-182. <https://doi.org/10.1080/00221686.2018.1478895>
- [7] Alauddin, M. & Tsujimoto, T. (2012). Optimum configuration of groynes for stabilization of alluvial rivers with fine sediments. *International Journal of Sediment Research*, 27(2), 158-167. [https://doi.org/10.1016/s1001-6279\(12\)60024-9](https://doi.org/10.1016/s1001-6279(12)60024-9)
- [8] Mukherjee, A. & Sarma, A. K. (2011). *2D Flow Simulation in Alluvial River using MIKE Software: A modelling approach*.
- [9] Bahrami-Yarahmadi, M., Pagliara, S., Yabarehpour, E., & Najafi, N. (2020). Study of scour and flow patterns around triangular-shaped spur dikes. *KSCE Journal of Civil Engineering*, 24(11), 3279-3288. <https://doi.org/10.1007/s12205-020-2261-x>
- [10] Tritthart, M., Glas, M., Liedermann, M., & Habersack, H. (2014). Numerical study of morphodynamics and ecological parameters following alternative groyne layouts at the Danube River. *ICHE 2014. Proceedings of the 11th International Conference on Hydrosience & Engineering*, 685-692.
- [11] Ghodsian, M. & Vaghefi, M. (2009). Experimental study on scour and flow field in a scour hole around a T-shape spur dike in a 90° Bend. *International Journal of Sediment Research*, 24(2), 145-158. [https://doi.org/10.1016/s1001-6279\(09\)60022-6](https://doi.org/10.1016/s1001-6279(09)60022-6)
- [12] Haider, R., Qiao, D., Yan, J., Ning, D., Pasha, G. A., & Iqbal, S. (2022). Flow characteristics around permeable spur dike with different staggered pores at varying angles. *Arabian Journal for Science and Engineering*, 47(4), 5219-5236. <https://doi.org/10.1007/s13369-021-06435-4>
- [13] Haider, R., Qiao, D., Wang, X., Yan, J., & Ning, D. (2022). Role of grouped piles on flow characteristics around impermeable spur dike. *International Journal of Civil Engineering*, 20(8), 869-883. <https://doi.org/10.1007/s40999-022-00706-3>
- [14] Pasha, G. A., Ghumman, A. R., Naseer, M. J., Iqbal, S., & Ahmed, A. (2022). Flow characteristics in a two-stage vegetated compound trapezoidal channel. *Iranian Journal of Science and Technology, Transactions of Civil Engineering*. <https://doi.org/10.1007/s40996-022-00904-y>
- [15] Anjum, N. & Tanaka, N. (2019). Hydrodynamics of longitudinally discontinuous, vertically double layered and partially covered rigid vegetation patches in open channel flow. *River Research and Applications*, 36(1), 115-127. <https://doi.org/10.1002/rra.3546>
- [16] El-Rashedy, S. F., Ezzeldin, M. M., & Sarhan, T. A. (2016). Influence of spur dikes shapes on scour characteristics. *International Journal of Scientific Engineering Research*, 9(6), 1285-1301.
- [17] Nayyer, S., Farzin, S., Karami, H., & Rostami, M. (2019). A numerical and experimental investigation of the effects of combination of spur dikes in series on a flow field. *Journal of the Brazilian Society of Mechanical Sciences and Engineering*, 41(6). <https://doi.org/10.1007/s40430-019-1757-0>
- [18] Nayyer, S., Farzin, S., Karami, H., & Rostami, M. (2019). A numerical and experimental investigation of the effects of combination of spur dikes in series on a flow field. *Journal of the Brazilian Society of Mechanical Sciences and Engineering*, 41(6). <https://doi.org/10.1007/s40430-019-1757-0>
- [19] Brevis, W., García-Villalba, M., & Niño, Y. (2014). Experimental and large Eddy Simulation Study of the flow developed by a sequence of lateral obstacles. *Environmental Fluid Mechanics*, 14(4), 873-893. <https://doi.org/10.1007/s10652-013-9328-x>
- [20] Han, X., Lin, P., & Parker, G. (2018). The 3D Numerical Study on Flow and Sediment Properties of a River with Grouped Spur Dikes. *E3S Web of Conferences*, 40. <https://doi.org/10.1051/e3sconf/20184005056>
- [21] Koken, M. & Constantinescu, G. (2008). An investigation of the flow and scour mechanisms around isolated spur dikes in a shallow open channel: 1. conditions corresponding to the initiation of the erosion and deposition process. *Water Resources Research*, 44(8). <https://doi.org/10.1029/2007wr006489>
- [22] Wu, T. & Qin, J. (2020). Influence of flow and sediment transport processes on sedimentation in Groyne Fields. *Journal of Coastal Research*, 95(sp1), 304. <https://doi.org/10.2112/si95-059.1>
- [23] Koken, M. (2011). Coherent structures around isolated spur dikes at various approach flow angles. *Journal of Hydraulic Research*, 49(6), 736-743. <https://doi.org/10.1080/00221686.2011.616316>
- [24] Koken, M. & Gogus, M. (2014). Effect of spur dike length on the horseshoe vortex system and the bed shear stress distribution. *Journal of Hydraulic Research*, 53(2), 196-206. <https://doi.org/10.1080/00221686.2014.967819>
- [25] Herrera-Granados, O. (2018). Turbulence flow modeling of one-sharp-groyne field. *GeoPlanet: Earth and Planetary Sciences*, 207-218. https://doi.org/10.1007/978-3-319-70914-7_12
- [26] Kang, J., Yeo, H., Kim, S., & Ji, U. (2011). Permeability effects of single groin on flow characteristics. *Journal of Hydraulic Research*, 49(6), 728-735. <https://doi.org/10.1080/00221686.2011.614520>
- [27] Kang, J., Yeo, H., Kim, S., & Ji, U. (2011). Permeability effects of single groin on flow characteristics. *Journal of Hydraulic Research*, 49(6), 728-735. <https://doi.org/10.1080/00221686.2011.614520>
- [28] Najafi Birgani, N., Shafai Bejestan, M., & Bahrami Yarahmadi, M. (2020). Experimental Investigation of the Performance of Triangular Vanes on Bed Topography in Straight Rivers. *Water and Soil Science*, 30(2), 91-102.
- [29] Versteeg, H. & Malalasekera, W. (2007). *An introduction to computational fluid dynamics*. Prentice Hall.
- [30] Ahmad, M., Ghani, U., Anjum, N., Ahmed Pasha, G., Kaleem Ullah, M., & Ahmed, A. (2020). Investigating the flow hydrodynamics in a compound channel with layered vegetated floodplains. *Civil Engineering Journal*, 6(5), 860-876. <https://doi.org/10.28991/cej-2020-03091513>
- [31] Anjum, N. & Tanaka, N. (2019). Numerical investigation of velocity distribution of turbulent flow through vertically double-layered vegetation. *Water Science and Engineering*, 12(4), 319-329. <https://doi.org/10.1016/j.wse.2019.11.001>
- [32] Koutrouveli, T. I., Dimas, A. A., Fourniotis, N. T., & Demetropoulos, A. C. (2018). Groyne spacing role on the effective control of wall shear stress in open-channel flow. *Journal of Hydraulic Research*, 57(2), 167-182. <https://doi.org/10.1080/00221686.2018.1478895>
- [33] Weitbrecht, V., Socolofsky, S. A., & Jirka, G. H. (2008). Experiments on mass exchange between groin fields and main stream in Rivers. *Journal of Hydraulic Engineering*,

- 134(2), 173-183.
[https://doi.org/10.1061/\(asce\)0733-9429\(2008\)134:2\(173\)](https://doi.org/10.1061/(asce)0733-9429(2008)134:2(173))
- [34] Molinas, A., Kheireldin, K., & Wu, B. (1998). Shear stress around vertical wall abutments. *Journal of Hydraulic Engineering*, 124(8), 822-830.
[https://doi.org/10.1061/\(asce\)0733-9429\(1998\)124:8\(822\)](https://doi.org/10.1061/(asce)0733-9429(1998)124:8(822))
- [35] Vaghefi, M., Safarpour, Y., & Akbari, M. (2017). Numerical comparison of the parameters influencing the turbulent flow using a T-shaped spur dike in a 90° Bend. *Journal of Applied Fluid Mechanics*, 10(1), 231-241.
<https://doi.org/10.18869/acadpub.jafm.73.238.26175>
- [36] Basser, H., Karami, H., Shamshirband, S., Akib, S., Amirmojahedi, M., Ahmad, R., Jahangirzadeh, A., & Javidnia, H. (2015). Hybrid ANFIS–PSO approach for predicting optimum parameters of a protective spur dike. *Applied Soft Computing*, 30, 642-649.
<https://doi.org/10.1016/j.asoc.2015.02.011>
- [37] Sadat, S. H. & Tominaga, A. (2015). Optimal distance between pile-group and spur-dike to reduce local scour. *Journal of Japan Society of Civil Engineers, Ser. B1 (Hydraulic Engineering)*, 71(4).
https://doi.org/10.2208/jscejhe.71.i_187
- [38] Zhang, H., Nakagawa, H., Muto, Y., Muramoto, Y., & Touchi, D. (2007). Bed deformation around groins in a river restoration project. *Proceedings of Hydraulic Engineering*, 51, 127-132. <https://doi.org/10.2208/prohe.51.127>
- [39] Atarodi, A., Karami, H., Ardeshir, A., Hosseini, K., & Lampert, D. (2020). Experimental investigation of scour reduction around spur dikes by collar using Taguchi method. *Iranian Journal of Science and Technology, Transactions of Civil Engineering*, 45(2), 971-983.
<https://doi.org/10.1007/s40996-020-00373-1>

Contact information:

Sohail IQBAL, PhD student
 Dept. of Civil Engineering,
 University of Engineering and Technology,
 Taxila 47050, Pakistan
 E-mail: sohailsakhani147@gmail.com

Ghufran Ahmed PASHA, PhD Assistant Professor
 (Corresponding Author)
 Dept. of Civil Engineering,
 University of Engineering and Technology,
 Taxila 47050, Pakistan
 E-mail: ghufran.ahmed@uettaxila.edu.pk

Usman GHANI, PhD Professor
 Dept. of Civil Engineering,
 University of Engineering and Technology,
 Taxila 47050, Pakistan
 E-mail: usman.ghani@uettaxila.edu.pk

Afzal AHMED, PhD Lecturer
 Dept. of Civil Engineering,
 University of Engineering and Technology,
 Taxila 47050, Pakistan
 E-mail: afzal.ahmed@uettaxila.edu.pk

Rashid FAROOQ, PhD Assistant Professor
 Department of Civil Engineering,
 International Islamic University,
 H-10, Islamabad 44000, Pakistan
 E-mail: rashidmeo50@gmail.com

Rizwan HAIDER, Masters student
 State Key Laboratory of Coastal and Offshore Engineering,
 Dalian University of Technology,
 Dalian 116024, China
 E-mail: rizwanhaider@mail.dlut.edu.cn